Tropical volcanic eruptions enhance Pacific-driven global tropical cyclone genesis

ENVIRONMENTAL RESEARCH
LETTERS

PURPOSE-LED PUBLISHING™

Part of the
ENVIRONMENTAL RESEARCH
SERIES

LETTER • OPEN ACCESS

Tropical volcanic eruptions enhance Pacific-driven global tropical cyclone genesis

To cite this article: Jiuwei Zhao *et al* 2025 *Environ. Res. Lett.* **20** 084040

ENVIRONMENTAL RESEARCH
LETTERS

OPEN ACCESS

RECEIVED
15 May 2025

REVISED
15 June 2025

ACCEPTED FOR PUBLICATION
26 June 2025

PUBLISHED
8 July 2025

LETTER

Tropical volcanic eruptions enhance Pacific-driven global tropical cyclone genesis

Jiuwei Zhao[1], Ruifen Zhan[2,*], Yue Li[1], Yuqing Wang[3], Weiyi Sun[4], Xiangbo Feng[5] and Shanshan Liu[1]

[1] State Key Laboratory of Climate System Prediction and Risk Management (CPRM)/Collaborative Innovation Center on Forecast and Evaluation of Meteorological Disasters (CIC-FEMD), Nanjing University of Information Science & Technology (NUIST), Nanjing, People's Republic of China
[2] Department of Atmospheric and Oceanic Sciences & Institute of Atmospheric Sciences, Fudan University, Shanghai, People's Republic of China
[3] Department of Atmospheric Sciences and International Pacific Research Center, School of Ocean and Earth Science and Technology, University of Hawaii at Manoa, Honolulu, United States of America
[4] State Key Laboratory of Climate System Prediction and Risk Management/Key Laboratory for Virtual Geographic Environment of Ministry of Education, Nanjing Normal University, Nanjing, People's Republic of China
[5] National Center for Atmospheric Science (NCAS), University of Reading, Reading, United Kingdom
[*] Author to whom any correspondence should be addressed.

E-mail: Zhanrf@fudan.edu.cn

Keywords: tropical volcanic eruptions, tropical cyclone genesis frequency, El Niño-like SST pattern, Walker circulation

Supplementary material for this article is available online

Abstract

Whether, and to what extent, strong tropical volcanic eruptions (TVEs) affect global tropical cyclone (TC) genesis frequency (TCGF) remains uncertain. Here, we address this issue using both high-resolution reanalysis data and large ensemble simulations. We find a significant increase in TCGF over the Pacific within two years following TVEs, while a statistically insignificant decrease over the South Indian Ocean, leading to an overall increase in global TCGF driven mainly by Pacific basin responses. Strong TVEs suppress precipitation over the Maritime Continent and lower global mean sea surface temperature (SST), while inducing warming in the equatorial central Pacific, resulting in an El Niño-like SST pattern. These anomalies weaken the Walker Circulation and drive low-level westerly wind and upper-level easterly wind anomalies over the tropical Pacific, creating favorable conditions for enhanced Pacific TCGF. These results offer new insights into how TVEs influence TC activity on both global and regional scales.

1. Introduction

Tropical cyclone (TC) activity is regulated by a variety of internal variabilities and external forcings. Over the past few decades, significant attention has been given to understanding how these factors influence TC activity, particularly in terms of TC genesis frequency (TCGF) across various basins (Walsh *et al* 2015, Emanuel 2018, Zhao *et al* 2022). Most of previous studies have focused on the influence of atmospheric and oceanic internal variabilities on TCGF, spanning from interannual to decadal and multi-decadal scales (Wang and Chan 2002, Li *et al* 2015, Patricola *et al* 2016, Zhang *et al* 2017, 2018, Zhao *et al* 2018, Murakami *et al* 2020, Sobel *et al* 2021). In addition, anthropogenic forcing has been shown to induce basin-dependent TCGF changes (Murakami *et al* 2012, 2013, 2018, Knutson *et al* 2019, Zhao *et al* 2020a, 2020b, Chand *et al* 2022). However, as a natural source of climate variability, the influence of tropical volcanic eruptions (TVEs) on global TCGF remains inconclusive and contentious, highlighting a critical gap in our understanding of TC activity in the context of natural climate variability (Camargo and Polvani 2019, Benton *et al* 2022).

TVEs typically inject a large amount of sulfate aerosol particles into the stratosphere, reflecting downward solar radiation, which consequently leads to the decrease in sea surface temperature (SST), modulating associated large-scale circulations (Nicholls 1988, Pausata and Camargo 2019, Fadnavis *et al* 2021, Zhou *et al* 2023). Previous studies have extensively discussed the influence of TVEs on global TCGF through their modulation of atmospheric and oceanic circulations, particularly with respect to TCGF in the North Atlantic (Guevara-Murua *et al* 2015, Altman *et al* 2021, Dogar *et al* 2023, Zhou *et al* 2023). Some studies have suggested that TVEs suppress global or regional TCGF due to decreased SST and modified phase of the El Niño-Southern Oscillation (ENSO) (Emanuel and Nolan 2004, Yan *et al* 2017). Particularly, some studies found a significant decrease in North Atlantic TCGF following strong TVEs (Evan 2012, Guevara-Murua *et al* 2015, Chiacchio *et al* 2017). However, these results were potentially contaminated by contributions from El Niño variability in observation (Patricola *et al* 2016, Camargo and Polvani 2019). Recent studies have also pointed out that no evidence supports a decrease in TCGF following TVEs (Camargo and Polvani 2019, Benton *et al* 2022). This inconsistency underscores the need to clarify the role of TVEs in modulating global TCGF.

Various mechanisms have been proposed to explain the atmospheric and oceanic circulation changes following TVEs. One of the most significant impacts of volcanic eruptions is a decrease in global mean SST. The rate of SST cooling is highly latitude-dependent, including an inter-hemispheric asymmetry, which can lead to a meridional shift of the intertropical convergence zone (Pausata and Camargo 2019) and diverse changes in TC activity (Yan *et al* 2017, 2019). Specifically, TVEs could also induce drought in India and reduce tropical precipitation. The redistribution of heating sources further alters monsoon systems (Paik *et al* 2020, Chen *et al* 2022, Liu *et al* 2022, Zhou *et al* 2023), which can subsequently lead to changes in regional TCGF. However, whether monsoon circulation intensifies or shows a basin-dependence after TVEs remains under debate (Robock 2000, Iles *et al* 2013, Liu *et al* 2016, Zhou *et al* 2021, 2022, 2023). Many studies argued that TVEs can trigger El Niño events in the following 1–2 years by inducing strong equatorial westerly wind anomalies (Khodri *et al* 2017, Eddebbar *et al* 2019, Chai *et al* 2020, Dogar *et al* 2023). Nonetheless, recent studies based on paleoclimate simulations have suggested that changes in the occurrence of El Niño events following TVEs is insignificant and depends largely on the preconditions of oceanic states, eruption timing, and the amount of volcanic sulfate aerosols (Liu *et al* 2018, Predybaylo *et al* 2020, Zhu *et al* 2022).

Currently, confidence is lacking in depicting global TCGF changes in response to TVEs based on observations due to the co-existence of multiscale climate modes affecting TCGF and the limited observational records available. Although numerical ensemble simulations using global climate models are often used to detect the TVE effects, they could not reliably capture TC activity due to their relatively coarse model resolutions. In this study, we analyzed two major TVE events (El Chichón in 1982 and Pinatubo in 1991) using both reanalysis data and high-resolution large ensemble simulations. The Agung eruption in 1963 was excluded because of unreliable TC best-track data prior to 1980, especially in the Southern Hemisphere. We will show that a clear increase in global TCGF following TVEs can be detected from observations after removing the effects of internal climate variabilities, such as ENSO (Jin 1997, Jin *et al* 2014), Interdecadal Pacific Oscillation (IPO; Li *et al* 2015, 2018, Zhao *et al* 2020b), and Atlantic Multi-decadal Oscillation (AMO; Zhang *et al* 2018, Song *et al* 2022, Zhao *et al* 2022). Furthermore, high-resolution large ensemble simulations confirm a robust increase in global TCGF resulting from the weakening of the Walker circulation associated with the reduced precipitation over the Maritime Continent.

2. Data and methodology

2.1. TC best-track data and reanalysis datasets

In this study, we used the TC best-track data from the International Best Track Archive for Climate Stewardship (IBTrACS) for 1950–2010, which contain 6 h TC center (longitude and latitude) and intensity (maximum-sustained surface wind) information (Knapp *et al* 2010). The TC genesis location was defined when its surface wind speed first reached or exceeded 35 knots (about 17.2 m s^{-1}) during its lifespan. The TCGF during 1950–2010 was summed during the TC season from June to November for the Northern Hemisphere and from December to the following April (1950–2011) for the Southern Hemisphere. Before 1980, Southern Hemisphere TCGF was derived from ERA5 data, while Northern Hemisphere TCGF was compared with corresponding ERA5 values. The TC best-track dataset for the Northern Hemisphere, excluding the Indian Ocean, was obtained from the Joint Typhoon Warning Center. Due to frequent data gaps, TC records in the Southern Hemisphere and North Indian Ocean before 1980 are considered less reliable. Therefore, the 1963 Agung eruption was not considered in this study. We thus focus on the two more recent events, namely Pinatubo and El Chichón eruptions. Also, the TCGF after removing the 11-year running mean for the Southern Hemisphere is derived from the ERA data to substitute the TCGF in observation before 1980 although we did not analyze the TVE impact of Agung.

We used the monthly atmospheric data, including 850 hPa and 200 hPa winds, from the ERA5 (Hersbach *et al* 2020) with a horizontal resolution interpolated to 2.5°. The 6 h ERA5 data, including surface wind speed, sea level pressure (SLP), 850 hPa vorticity and 500–300 hPa averaged temperature, are used to derive the TCGF in ERA5 reanalysis. The monthly SST data were derived from the National Oceanic and Atmospheric Administration (NOAA) (Huang *et al* 2017) and Hadley Centre Sea Ice and SST (HadISST) (Rayner *et al* 2003) with the horizontal resolution interpolated into 1° × 1°. The precipitation data were obtained from the Global Precipitation Climatology Project (Huffman *et al* 1997, 2023).

2.2. NOAA-20C large ensemble reanalysis

The observed TCGF only contains two volcanic eruption cases. To reduce the randomness and uncertainty induced by low sample size, we further used a large ensemble dataset for twentieth century (20C) from NOAA. The version 3 of NOAA-20C assimilated observed (reported) SLP to the model and generated 80 ensemble members by slightly perturbating the SLP (Slivinski *et al* 2019). This new version of NOAA-20C has a horizontal resolution of total spheric wavenumber 254 (about 50 km) and a 6 h interval, which can be used to explicitly extract the TC-like vortices based on tracking algorithm (Hodges *et al* 2017). We analyzed the derived TCGF across 80 ensemble members from 1970–2010.

2.3. Large ensemble simulations from Geophysical Fluid Dynamic Laboratory (GFDL) and community earth system model (CESM)

We used large ensemble simulations by two global climate modeling centers to assess the TCGF change in response to volcanic eruptions. The first large ensemble simulations are based on the SPEAR model developed by the GFDL, which is a new generation seamless model for synoptic to multi-decadal simulations, predictions and projections (Delworth *et al* 2020, Lu *et al* 2020, Xiang *et al* 2022). The model physics, including parameterized schemes, are renowned with the improved capability to simulate intraseasonal variability (Xiang *et al* 2022). The dynamic core of cubic spheres in SPEAR is inherited from the previous version of high-resolution atmospheric model in GFDL (Zhao *et al* 2009). It has an approximate horizontal resolution of 0.5° with 576 × 360 grids, enabling it to resolve the TC-like vortices reasonably. Previous studies have demonstrated that SPEAR can well simulate the climatological distribution of TCGF and multiscale variabilities under realistic boundary forcing (Delworth *et al* 2020, Lu *et al* 2020). The historical runs of the SPEAR model, covering 1921–2014, were forced by reconstructed stratospheric aerosol data and greenhouse gas (GHG) concentrations, consistent with the Coupled Model Intercomparison Project (CMIP) protocols (Eyring *et al* 2016, Haarsma *et al* 2016). Unlike CMIP, SPEAR includes 30 ensemble members, each initialized differently but using the same aerosol and GHG concentrations. The daily-averaged surface wind and SLP data during 1921–2014 are used in this study to detect the TC information (see the TC detection algorithm in Method), and the monthly SST, precipitation, and winds data are used to analyze the circulation changes induced by volcanic eruptions. Note that both of strong TVEs occurred well before 2014. Therefore, the limitation of simulation data to 2014 does not affect our analysis or conclusions.

We also recalculated the annual mean SST and TCGF from 1940–2010 in a previous study based on Forecast-oriented Low Ocean Resolution models with and without flux adjustment (FLOR-FA and FLOR), and SPEAR model in GFDL (Murakami *et al* 2020). The three models from GFDL provide 95 ensemble members with FLOR, FLOR-FA and SPEAR each containing 35, 30 and 30 ensemble members. The models have two scenarios that one is natural forcing experiment that only the volcano-induced aerosols are added in the simulations and the other is All Forcing experiment that both anthropogenic GHG and volcano-induced aerosols are added as the external forcing (Murakami *et al* 2020).

The second large ensemble simulations are from the CESM developed by the National Centers for Atmospheric Research (NCAR) (Hurrell *et al* 2013, Danabasoglu *et al* 2020). Its dataset is used to verify the results based on the dataset from SPEAR. The CESM has different groups of ensemble simulations for various research purposes. We also adopted the historical run with 35 ensemble members. CESM1 has a horizontal resolution of 0.9° × 1.25°, which is relatively coarse for detecting TC-like vortices. However, CESM1 provides 6 h instantaneous wind data for 1990–2005 and the monthly data of SST and winds for 1921–2005. This allows us to analyze the 1991 volcanic eruption. Notably, the instantaneous wind speeds in TCs are usually stronger than the 6 h averaged and daily mean values. We used the 850 hPa instantaneous winds to derive the TC-like vortices. Although the CESM1 underestimated the climatological TCGF compared to the observations and the SPEAR, its simulated spatial distribution of TCGF is reasonable.

2.4. TC detection algorithm and spatial distribution of TCGF

In this study, we used the TC detection algorithm provided by the GFDL (www.gfdl.noaa.gov/tstorms/) to extract the TC-like vortices in the ERA5, NOAA-20C, SPEAR and CESM datasets (Zhao *et al* 2009, Murakami and Wang 2010, 2023).

As in our previous studies (Song *et al* 2022, Zhao *et al* 2022), we defined TCGF as the number of TCs generated in an area of 20° in longitude and 10° in latitude centered at a given grid point of 1° by 1° resolution.

2.5. Definitions of ENSO, IPO and AMO

The SST data were derived from HadISST. Here, we first removed the annual mean from 1950–2010 data, and then removed the linear trend. The monthly ENSO index was calculated based on the averaged SST in the Niño3.4 region (120°–170° W; 5° S–5° N). For the Northern Hemisphere, the annual ENSO index was averaged from June to November, while for the Southern Hemisphere, it was averaged from December to April of the following year. The monthly IPO index was downloaded from https://psl.noaa.gov/data/timeseries/IPOTPI/, and the monthly AMO index from https://psl.noaa.gov/data/timeseries/AMO/.

2.6. Removal of ENSO, IPO and AMO signals in observations

TCGF is modulated by internal oceanic modes across interannual to interdecadal timescales (Wang and Chan 2002, Vimont and Kossin 2007, Jin *et al* 2014, Li *et al* 2015, Zhang *et al* 2018, Zhao *et al* 2018, Murakami *et al* 2020). To minimize their influences, we sequentially removed ENSO, IPO and AMO signals from the observational data, following methods outlined in previous studies (Ashok *et al* 2003, Zhao *et al* 2016). Note that we removed the monthly signals of oceanic factors to analyze the monthly evolution of global mean SST.

2.7. Definitions of global mean SST and strong TVEs

To quantify the TVE impact on global mean SST, we defined global mean SST as the SST averaged between 60° S and 60° N, excluding higher latitudes potentially covered by sea ice. In the simulations, we presented the global mean SST anomalies during 1921–2014 (1921–2005 for CESM) with the baseline fixed as the climatological mean during 1921–1950. We also applied an 11-year running mean to minimize the warming trend in historical high-resolution large ensemble simulations since 1980s. In the observations, the original global mean SST anomalies are derived by sequentially removing the monthly climatology and linear trend from 1960 to 2020. The modified global mean SST anomalies are obtained after removing the oceanic modes as introduced above.

In this study, strong TVEs are defined as those with a volcanic explosivity index $\geqslant 5$ and a stratospheric sulfate (SO_4) injection of at least 5–10 Tg. These thresholds are informed by the characteristics of major eruptions discussed in previous studies (Sato *et al* 1993, Robock 2000, Zanchettin *et al* 2016), and provide a consistent and objective basis for event selection in our analysis.

3. Results

3.1. TCGF increase in response to TVEs

Figure 1 shows the changes in SST and TCGF in response to the two strong TVEs since 1980. Generally, the global mean SST displays a weak positive anomaly before the TVE and evolves into negative afterwards based on both original (green) and signal-corrected (purple) time series (figures 1(a) and (b); supplementary figures 1(a) and (b)). However, the magnitude and duration of TVE-induced global mean SST anomalies vary between the two TVE events. The Pinatubo (120° E, 15° N) erupted on 15th June 1991, sustained until early September, and induced a strong negative global mean SST anomaly in 1992, while the 1991 summer SST changed little due to the short reaction time (figure 1(a)). In contrast, the El Chichón (93° W, 17° N) erupted in March 1982, which is half strong of the Pinatubo eruption, induced a negative global mean SST anomaly in the same year (June–September; figure 1(d)), with global mean SST quickly recovered in autumn of 1982. Due to notable SST cooling (∼0.17 °C), 1992 (for Pinatubo) and March–September 1982 (for El Chichón) were identified as periods of strong volcanic impact in the observations, as shown in figures 1(a) and (b) (shaded) and supplementary figures 1(a) and (b). SST anomalies also show distinct regional patterns in response to the eruptions (figures 1(c) and (d); supplementary figures 1(c) and (d)). Negative SST anomalies were observed in the Atlantic Ocean and western part of the North Pacific, and positive SST anomalies were mainly located in the tropical central to eastern Pacific in 1–2 years after the TVE events. These patterns show consistency in both spatial distribution and magnitude in SST change before and after removing the internal climate variabilities, including ENSO (Jin 1997, Jin *et al* 2014), IPO (Li *et al* 2015, Zhao *et al* 2018, 2020a, 2024), and AMO (Zhang *et al* 2018, Song *et al* 2022, Zhao *et al* 2022) and in different SST datasets (supplementary figure 1). Both the SPEAR from the GFDL and the CESM from the NCAR well reproduced the global mean SST decrease induced by the two events (figure 2). However, there are slight differences in the magnitude of negative global mean SST anomaly and the start time and duration of the TVE impact between reanalysis and the model simulations. In CESM, the SST response to TVEs is delayed by about one year relative to SPEAR (figure 2). Based on the response time of global mean SST cooling to the TVE, we consider 1982 in SPEAR and 1983 in CESM as the El Chichón influence (figure 2), while for the Pinatubo, we selected 1991–1992 in SPEAR and 1992–1993 in the CESM.

Remarkably, the global TCGF in 1992 reached 101—the highest observed during the study period of 1980–2010. This number is about 12.7 (figure 1(e); green dot) more than the mean from 1987 to 1997 in observation and around 13.7 (figure 1(e); orange median line) higher in 80-member ensemble mean of NOAA-20C (green line; figure 1(e)), with 12.8 (11.2) more in the Northern Hemisphere and 0.1 (2.5) less (more) in the Southern Hemisphere in respective observation and reanalysis (figures 1(f) and (g)). The number of observed global TCs in March–September for 1982 was about 5.7 (2.5) higher than the 11 year running mean in observation (simulations) with dominant contribution from Northern Hemisphere (figures 1(e) and (f)).

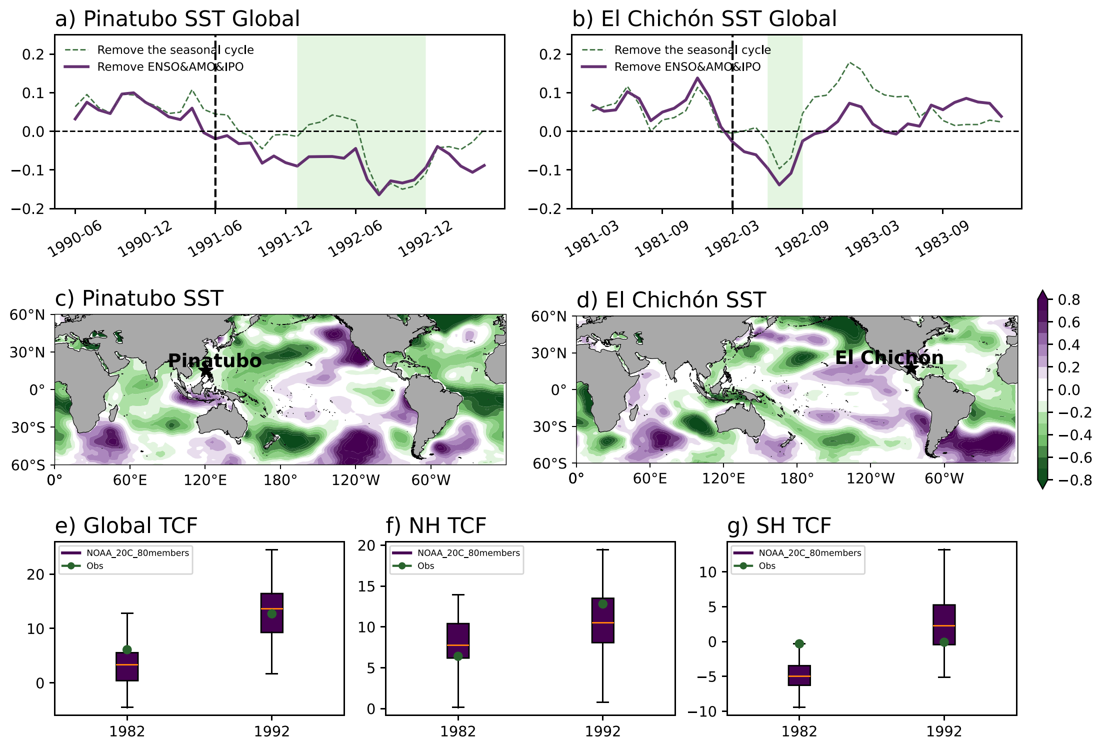

Figure 1. TVE impact on SST and TCGF over the globe. (a) Monthly evolution of Pinatubo SST anomaly with (purple) and without (green) the influence of oceanic modes removed; (b) monthly evolution of El Chichón SST anomaly; (c) the SST anomalies (averaged in 1992) after Pinatubo erupted, and (d) the El Chichón-related SST anomalies between March to September 1982; (e) box-and-whisker plot of global TCGF anomalies among 80 ensemble members of NOAA-20C reanalysis (purple) and in observation (green); (f) NH TCGF anomalies; and (g) SH TCGF anomalies. Here, the SST and TCGF in 1982 were calculated based on the average from March to September according to (b) while the SST and TCGF in 1992 were annually averaged referring from (a). The SST anomalies are obtained after removing oceanic internal variabilities (ENSO, IPO and AMO). The global TCGF was the sum of the NH and SH values. The box-and-whisker plot shows anomalous TCGF values of maximum, 75% percentile, median, 25% percentile and minimum across 80 ensemble members while the green dots represent the observed TCGF after removing the 11 year running mean.

Moreover, the observed TCGF is 3.6 higher in June–September for 1982, indicating that the TVE of El Chichón also contributes positively to the increase of TCGF.

Global anomalies of SST and TCGF in response to the TVEs are well reproduced by high-resolution large ensemble simulations (figure 3 and supplementary figure 2). The GFDL model reproduces the observed decrease in global mean SST, ranging from −0.2 °C to 0 °C (figures 3(a), 2 and supplementary figure 2), and the increase in the global TCGF following both TVE events (figure 3(b)). We further divided the globe into four regions in SPEAR model: North Pacific (NP; figure 3(c)), North Atlantic and North Indian Ocean (NAI; figure 3(d)) for the Northern Hemisphere, and Australia (AUS; figure 3(e)) and the South Indian Ocean (SIO; figure 3(f)) for the Southern Hemisphere. The TCGF in the NP, which accounts for 52.6% of the global TCGF during 1980–2010, shows an increase comparable to the global increase, thus contributing the most to the global TCGF increase in response to TVEs (figures 3(b) and (c)), consistent with observations (figures 1(e) and (f)). The NAI TCGF also increased dramatically following the two TVEs (figure 3(d)). In contrast, the TCGF in the Southern Hemisphere shows inconsistent changes between the two TVEs, with a seesaw between the SIO and AUS following the El Chichón eruption but consistent increase following the Pinatubo eruption (figures 3(e) and (f)). The former caused the insignificant change in global TCGF in 1982, while the latter led to the significant increase in 1992. Additionally, we examined the TCGF change induced by the Pinatubo eruption in the high-resolution large ensemble simulations from CESM. Similarly, TCGF shows a nearly global increase, except for a slight decrease in a small area in the SIO and eastern Pacific (supplementary figure 3).

We further explored the spatial patterns of TCGF anomalies in observation, reanalysis and high-resolution simulations (figure 4). For observation (figures 4(a) and (b)), in response to the Pinatubo eruption, a widespread enhancement of TCGF is seen across the western and eastern North Pacific, the North Indian Ocean, and the South Pacific east of Australia (figure 4(a)). In contrast, the SIO and

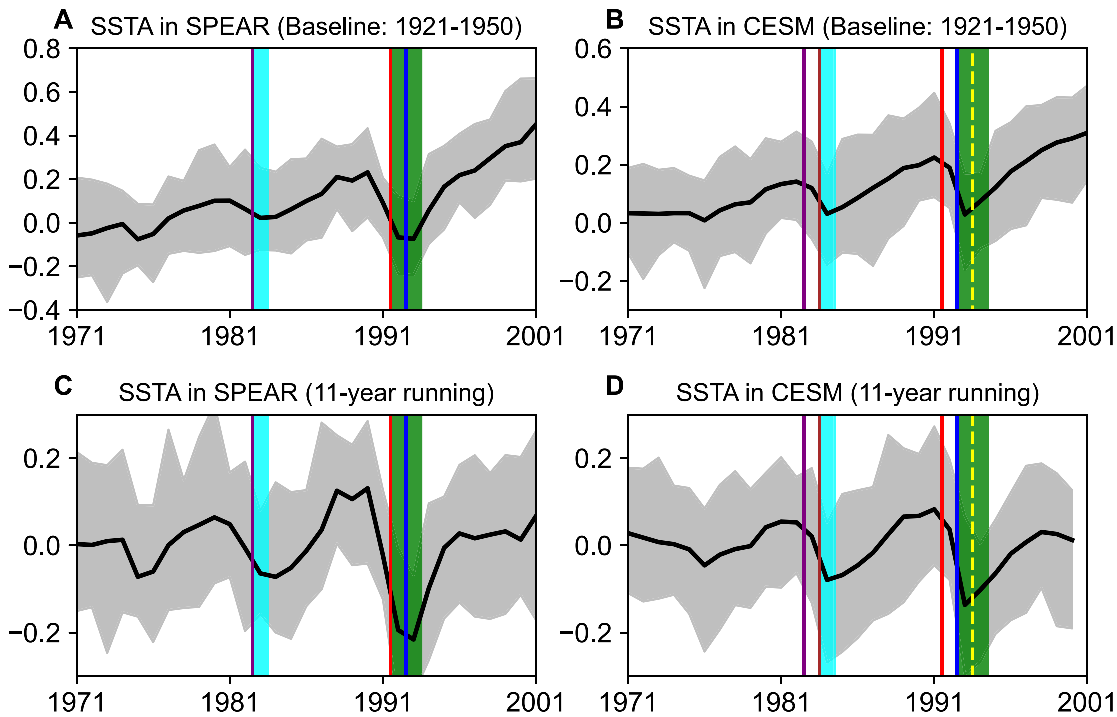

Figure 2. The GMSST anomalies from 1971–2001 in two HES. (a) The GMSST anomalies from 1921–2014 averaged between 60° S and 60° N compared with the climatological baseline from 1921–1950 in SPEAR model; (b) same as (a) but for the CESM model from 1921–2005; (c) the GMSST anomalies with a 11 year running window based on (a); and (d) same as (c) but for the CESM. The gray shading represents the model spread and the black line stands for the ensemble mean. The blue, cyan and green bars marked two TVE cases. The purple lines represent the eruption time of El Chichón in 1982 while the red lines represent the eruption time of Pinatubo in 1991. The shading of cyan stands for the influence time of El Chichón in 1982 in SPEAR model while 1982 in CESM model. The shadings of green indicate the volcanic influence time of Pinatubo between 1991–1992 in SPEAR model but 1992–1993 in CESM model.

the tropical Atlantic Ocean exhibit a decrease. The El Chichón eruption shows a broadly similar pattern with increased TCGF over the tropical Pacific and decreased activity over the SIO. However, the TCGF anomalies exhibit smaller magnitudes, and even show opposite pattern in the South Pacific east of Australia and the Atlantic Ocean north of 15° N (figure 4(b)).

These observed patterns are corroborated by the NOAA-20C reanalysis ensemble mean (figures 4(c) and (d)), which captures the spatial signatures of enhanced Pacific activity, and the suppressed activity in the SIO and the tropical Atlantic Ocean. This agreement strengthens confidence in the robustness of the volcanic impact on TC genesis. The model-simulated anomalies from the SPEAR large ensemble (figures 4(e) and (f)) further confirm these findings. Importantly, due to the large ensemble design, the internal climate variabilities such as ENSO, the IPO, and the AMO are strongly suppressed, allowing a more direct assessment of the volcanic forcing. In the model simulations, the TCGF increase over the tropical Pacific following the Pinatubo eruption is consistently reproduced, extending from the western to eastern North Pacific and into the South Pacific. Similarly, the response to El Chichón (figure 4(f)) also features enhanced TCGF over the Pacific, although the signal appears weaker than that for Pinatubo, potentially due to differences in eruption magnitude and background climate conditions. Furthermore, it is noteworthy that the simulated TCGF anomaly is stronger in 1991 than in 1992 (supplementary figure 4), indicating a prompt response in SPEAR model. In addition, analysis based on the relative importance of the Genesis Potential Index (Camargo *et al* 2007) suggests that the increase in TCGF anomaly is dominantly contributed by the dynamical factors, particularly enhanced low-level vorticity and reduced vertical wind shear (supplementary figure 5).

Previous studies have noted that TVEs often coincide with El Niño events (Nicholls 1988, Khodri *et al* 2017, Chai *et al* 2020, Dogar *et al* 2023). However, whether the volcano eruption directly trigger El Niño (Zhu *et al* 2022, Zhou *et al* 2023) or whether the observed TCGF changes result from El Niño or the TVE events remains a subject of debate (Evan 2012, Camargo and Polvani 2019). More importantly, in observation, 1991 is an El Niño developing year while 1992 is a neutral year. However, the 1992 TCGF is record-breaking high (figures 4(a) and (c)), which is mainly contributed by the increase of Pacific TCGF anomalies. It suggests a non-ENSO-related driver—likely volcanic in origin. The general consistency in spatial response patterns across observations, reanalysis, and simulations suggests a robust volcanic influence on TC genesis, particularly in the Pacific basin.

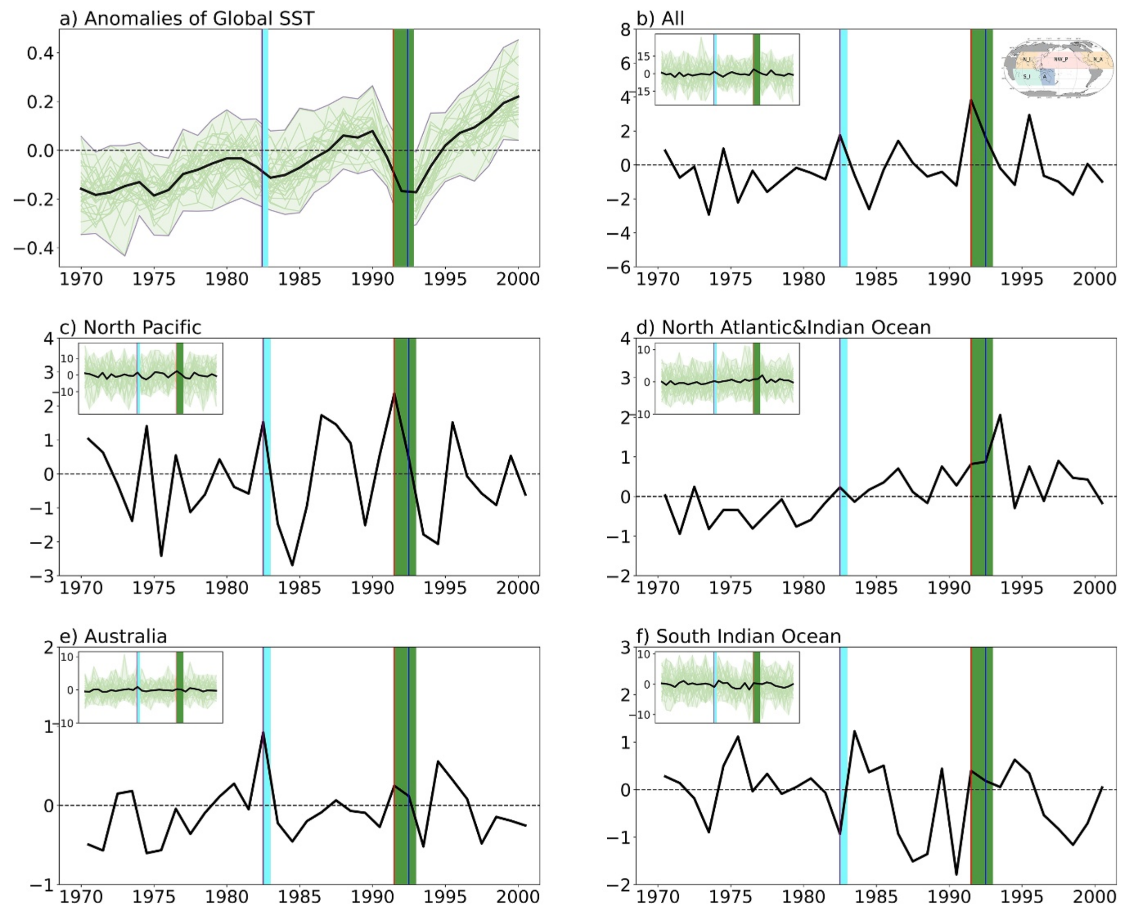

Figure 3. Global mean SST anomalies and TCGF from 1970 to 2000 in ensemble simulations. (a) Global mean SST anomaly; (b) global TCGF anomaly; (c) TCGF anomaly over the North Pacific; (d) TCGF anomaly over the North Atlantic and North Indian Ocean; (e) TCGF anomaly over Australia; and (f) TCGF anomaly over the South Indian Ocean. The shading in (a) represents the spread of SST anomalies simulated by 30 ensemble members, and the light colors in top left of (b)–(f) stand for the TCGF in 30 ensemble members. The subplots in the (b)–(f) enlarge the ensemble mean of TCGF anomaly for two TVE cases that are marked in top left.

3.2. Large-scale circulation changes in response to TVEs

To understand why the response in TCGF to the TVEs favors such a pattern as shown in figure 4, we analyzed circulation anomalies in response to the TVEs based on reanalysis data and SPEAR (figures 5, supplementary figures 6 and 7). Both reanalysis and high-resolution large ensemble simulations show that the easterly wind anomalies at the upper level dominate over the tropical Pacific. The low-level circulation shows a clear baroclinic response over the tropics, with the tropical westerly wind anomalies penetrating the entire Pacific region for both the Pinatubo and El Chichón events, while the Atlantic Ocean is dominated by easterly wind anomalies. This configuration is favorable for TC genesis over both the South and North Pacific for the Pinatubo and El Chichón (figure 4). Over the SIO, there is an anomalous cyclonic circulation over the western part and anticyclonic circulation over the eastern part for both Pinatubo and El Chichón (supplementary figures 6(b) and 7(d)), contributing to the dipole pattern in TCGF anomalies (figure 4).

Figures 5 and 6 also present SST and precipitation anomalies in response to the TVEs based on the ensemble averaged from SPEAR. Tropical precipitation shows a dramatic and region-dependent response to the TVEs. The TVEs induce significant negative precipitation anomalies over the Maritime Continent and a slight increase over the equatorial central and eastern Pacific. This is closely related to the decrease in precipitation over the Maritime Continent and the increase over the central Pacific. The ensemble mean SST anomaly was <0.5 °C, below the threshold for a central-Pacific El Niño. Nevertheless, El Niño-like SST pattern emerges, resulting in a significant weakening of the Pacific Walker circulation with low-level westerly wind anomalies and upper-level easterly wind anomalies (figure 5). The weakened Pacific Walker circulation is responsible for the significant increase in Pacific TCGF. The anti-Walker circulation over the Indian Ocean strengthens slightly, leading to a westward shift of the SIO TCGF region with a dipole pattern in TCGF anomalies, while the total TCGF changes are negligible. Since the

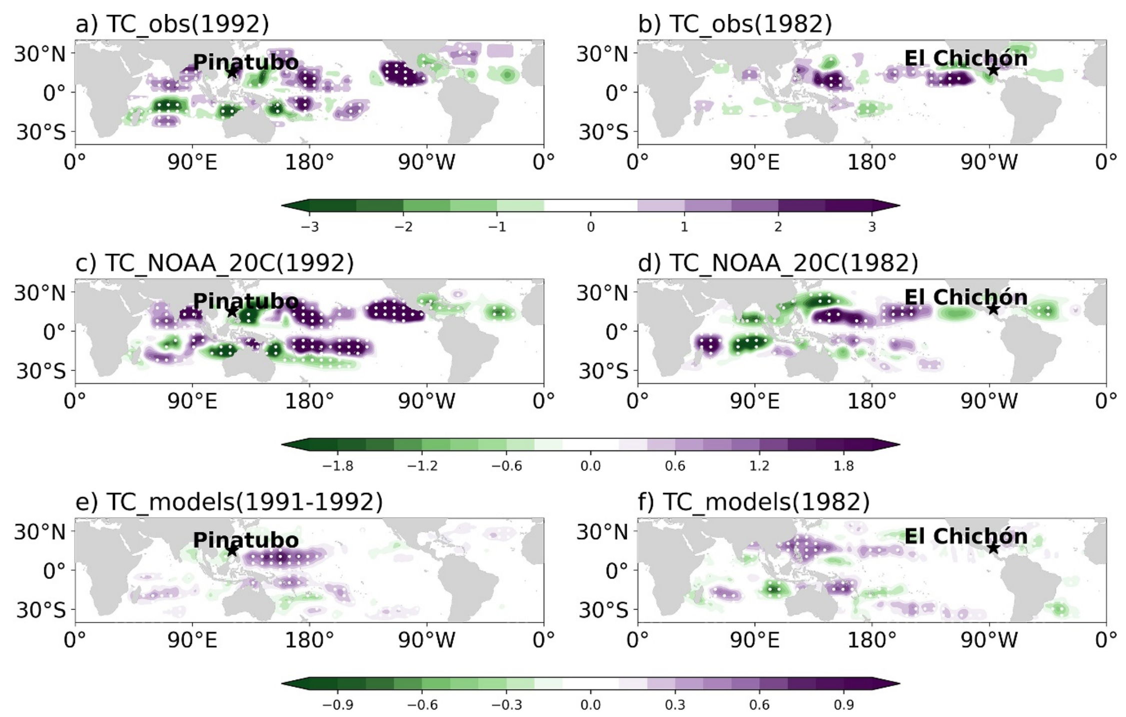

Figure 4. The observed, reanalyzed and simulated TCGF anomalies in response to the TVEs. (a) Observed TCGF anomaly in response to Pinatubo eruption; (b) observed TCGF anomaly induced by El Chichón eruption; (c) same as (a) but derived from 80-member ensemble mean reanalysis of NOAA-20C; (d) same as (b) but from NOAA-20C; (e) same as (a) but for the ensemble average in the SPEAR model; and (f) same as (b) but for the SPEAR model. The white dots represent area above the 90% confidence level based on Student's test.

TCGF over the Pacific contributes the most to the global TCGF, the TVEs induce a robust increase in Pacific TCGF, which dominates the increase in global TCGF.

3.3. Contribution of the TVE to TCGF change

Based on observation, the standard deviation of global TCGF is about 8.8. Notably, TCGF was 12.7 above the climatological mean after the Pinatubo eruption, indicating that the TVEs induced an increase exceeding 1.44 standard deviations. However, the observed TCGF changes induced by TVEs are also tangled with internal variability. Here, we further quantify the contribution of the TVEs to TCGF changes using the ensemble simulations (figure 7). We calculated the kernel density distribution across 30 ensemble members for the past 94 years using the SPEAR model (figures 7(a)–(c)). The historical global TCGF across these members shows a normal distribution with a median value of 80.2. In contrast, in response to TVE events, the median value rises to about 88, indicating that TVEs contribute 7.8 TCGF counts (figure 7(a)), close to one standard deviation (7.7) in SPEAR. This increase in global TCGF is dominantly contributed by that in the Northern Hemisphere (figure 7(b)), whereas the Southern Hemisphere shows weaker contributions, partly due to a seesaw pattern between TCGFs in the SIO and ASU (figure 3). To further elucidate the regional contributions, we analyzed the probability density functions of TCF over the Pacific including North and South Pacific (figure 7(d)). The results reveal a rightward shift in the distribution under TVEs, with the median TCF increasing by 4.1 (from 48.9 to 53). This regional increase accounts for approximately 44% of the global TCGF rise, reinforcing the Pacific as the primary region of TVE-induced TC activity enhancement.

4. Conclusions and discussion

In this study, we investigated the global TCGF response to recent TVEs and identified a robust increase in Pacific TCGF following the two TVE events, as evidenced by observations, reanalysis data, and high-resolution large ensemble simulations. While the TCGF changes over the Indian and Atlantic Oceans are inconsistent and statistically insignificant in both observations and simulations, the global TCGF shows a clear increase after the TVEs, which is dominantly contributed by that over the Pacific. This aligns with previous debates on whether these changes are linked to El Niño events (Camargo and Polvani 2019, Zhu *et al* 2022, Zhou *et al* 2023). After suppressing internal variabilities of ENSO, IPO and AMO, we revealed a consistent and robust increase

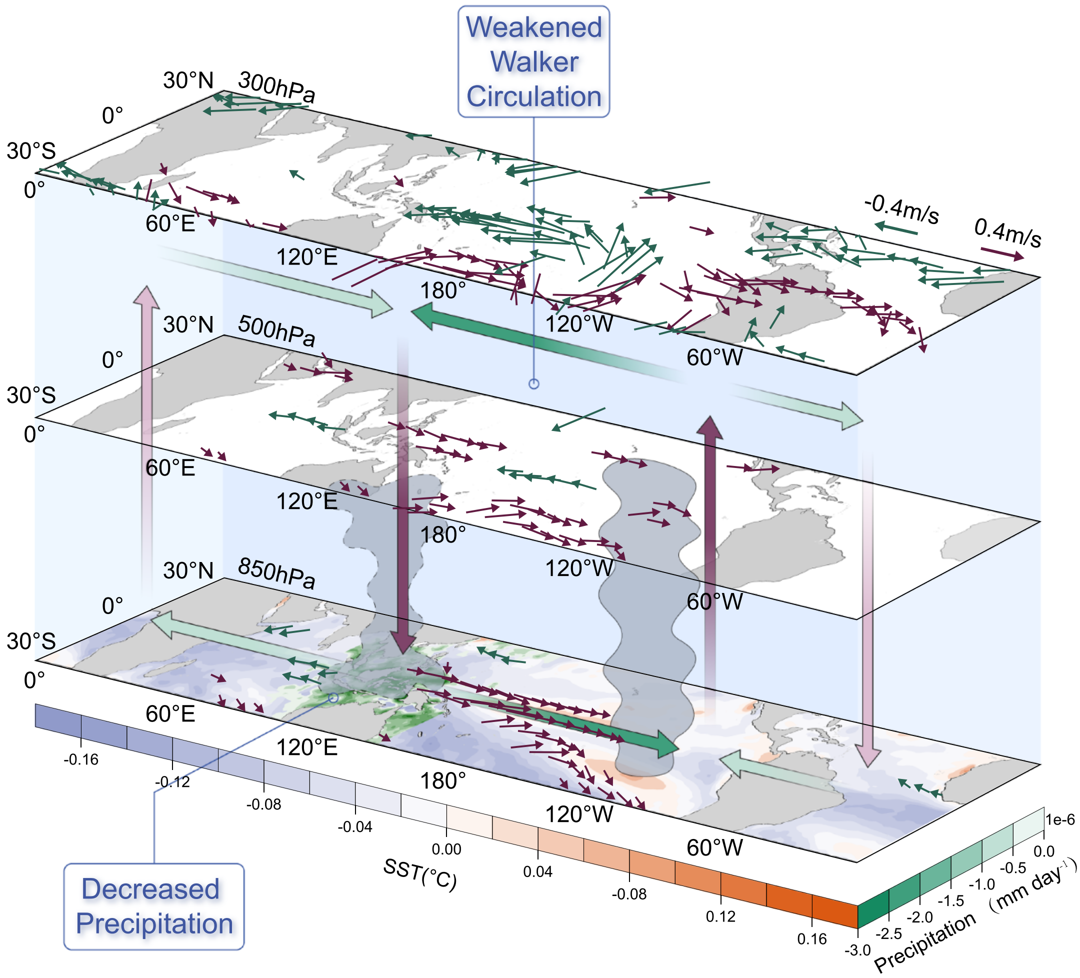

Figure 5. The TVE-induced wind anomalies at three different levels (300 hPa, 500 hPa and 850 hPa), and SST and precipitation anomalies based on the ensemble average of 30 members in SPEAR. At 850 hPa level, the blue and brown shading represents the SST anomalies induced by the TVE in the following 2 years; the green shading over the Maritime Continent represents the precipitation anomaly. The convection over the Maritime continent is significantly suppressed as pointed by the 'Decreased Precipitation', while it is enhanced over the central-eastern Pacific due to the El Nino-like tropical SST warming, which is represented by the clouds in gray color. This figure shows two cyclonic circulation anomalies over the respective NH and SH at 850 hPa, while anticyclonic circulation anomalies occur at 300 hPa, which favors TC genesis over the Pacific.

in TCGF. Further analysis shows that in these two strong cases, TVEs were associated with a significant decrease in precipitation over the Maritime Continent region, accompanied by a weak El Niño-like SST pattern. Consistent with a Matsuno-Gill-type response (Matsuno 1966, Gill 1980, Showman and Polvani 2010), these anomalies result in a significant weakening of the Pacific Walker circulation with low-level westerly wind anomalies and upper-level easterly wind anomalies, responsible for the significant increase in Pacific TCGF. Note that uncertainty remains in both simulated and observed TCGFs. Because the TCGF is less reliable before 1980, we did not consider the Agung eruption event in 1963. We noticed that the SIO TCGF is overestimated in ERA5 reanalysis, with values comparable to those over the western North Pacific. This conflicts with the climatological mean during 1980–2010, where SIO TCGF is substantially lower. Similar overestimation occurs in the SPEAR ensemble simulations, which attribute a disproportionately high contribution to SIO TCGF (supplementary figure 9). In contrast, ensemble simulations using CESM underestimates both Pacific and Atlantic TCGFs while overestimates the Southern Hemisphere TCGF contribution (supplementary figure 9). Despite these discrepancies, the impact of the Pinatubo eruption on the observed TCGF is more pronounced than that of El Chichón, largely due to its location and eruption strength. The Pinatubo eruption, which occurred near the Maritime Continent, is more likely to induce a substantial decrease in precipitation over the Pacific warm pool. This further trigger tropical westerly wind anomalies across the equatorial Pacific, inducing favorable conditions for an El Nino-like SST anomaly pattern over the tropical Pacific and TC genesis over the NP.

This study does not consider the contributions from land-based changes. Previous studies have

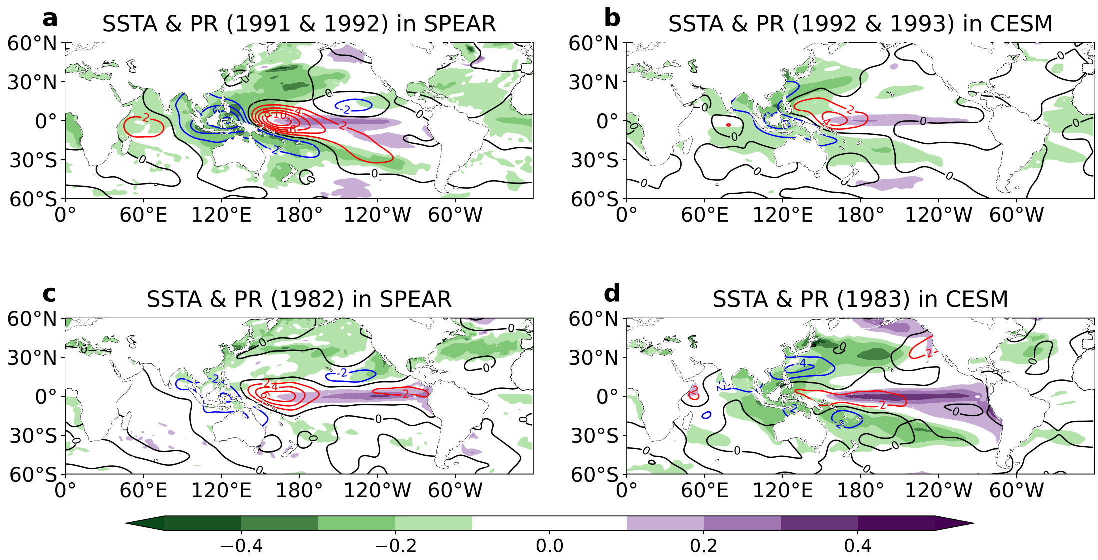

Figure 6. SST (shaded, unit: °C) and precipitation (contour, unit: mm) anomalies in response to TVE based on the ensemble averaged from the SPEAR and CESM models. (a) SST and precipitation anomalies in response to the 1991 Pinatubo TVE for the SPEAR (1991–1992); (b) same as (a), but for CESM (1992–1993); (c) SST and precipitation anomalies in response to the 1982 El Chichón occurred for the SPEAR (1982); (d) same as (c), but for CESM (1983).

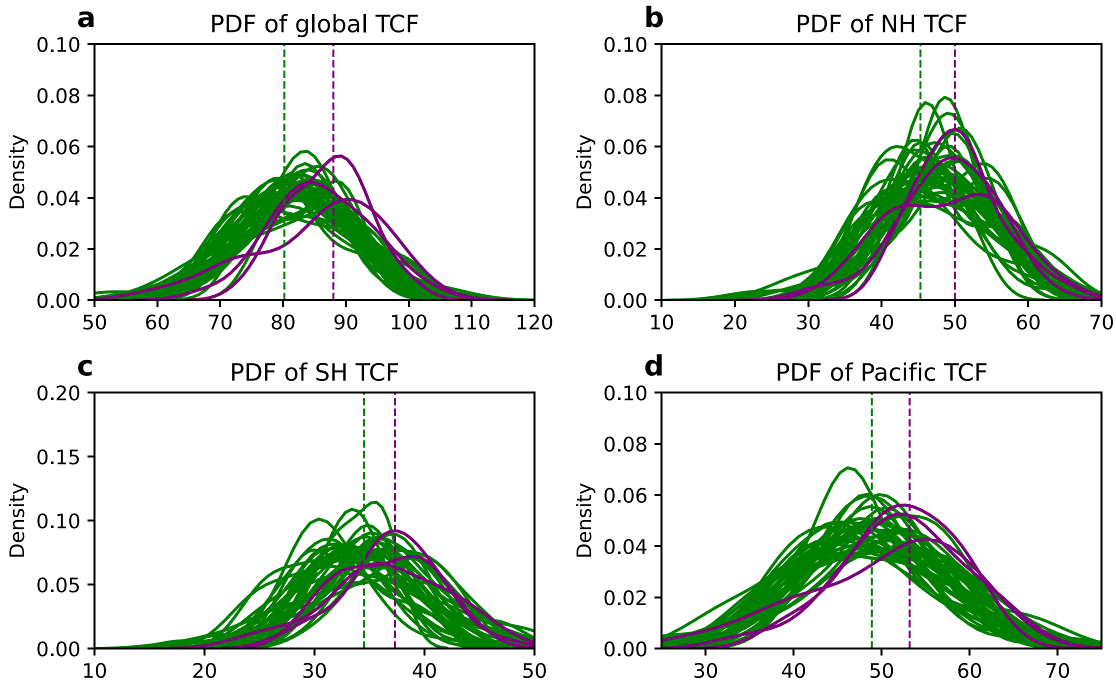

Figure 7. (a) The probability distribution function (PDF) of global TCF across 30 members with the purple lines standing for the years of TVEs; (b) same as (a) but for the Northern Hemisphere; (c) same as (a) but for the Southern Hemisphere; and (d) same as (a) but for the Pacific (North and South) regions.

pointed out that the land cools more than the ocean after TVEs, especially in tropical regions. The sulfate aerosols from the two TVEs directly suppressed precipitation in the Maritime Continent and western Pacific warm pool, regions already rich in precipitation. However, the impact of TVEs on the midlatitude land regions might be less pronounced. Future studies should examine how midlatitude volcanic eruptions, which can generate inter-hemispheric asymmetric responses in precipitation and SST, may cause a different response in global TCGF. Exploring these dynamics could provide deeper insights into the complex interactions between volcanic forcing, atmospheric responses, and TCGF.

These findings underscore the critical role of volcanic forcing in modulating TC activity through ocean–atmosphere coupling. The robust post-TVE increase in Pacific TCGF indicates that even short-lived external forcings can leave lasting imprints on regional and global atmospheric circulation. It reinforces the broader relevance of externally forced climate–cyclone interactions. TVE-induced SST and precipitation anomalies may influence low-frequency climate variability. These large-scale shifts can in turn affect long-term heat and moisture transport, with potential implications for global carbon fluxes, including changes in oceanic carbon uptake and terrestrial carbon storage. Collectively, our results highlight the importance of integrating TCs into Earth system frameworks to better understand climate–carbon feedbacks under episodic external forcings.

Data availability statement

In this study, the TC information data were downloaded from IBTrACS version 4 (www.ncei.noaa.gov/products/international-best-track-archive); the ECMWF reanalysis data is downloaded from https://cds.climate.copernicus.eu/cdsapp#!/dataset/reanalysis-era5-pressure-levels-monthly-means?tab=form, and the NCEP reanalysis (https://downloads.psl.noaa.gov/Datasets/ncep.reanalysis.derived/pressure/) is used to verify the consistency. The observations SST data can be requested from www.metoffice.gov.uk/hadobs/hadisst/data/download.html. The historical LENS outputs of SPEAR model can be downloaded from https://noaa-gfdl-spear-large-ensembles-pds.s3.amazonaws.com/index.html. And the CESM LENS data is from www.earthsystemgrid.org/dataset/ucar.cgd.ccsm4.cesmLE.atm.proc.6hourly_inst.U/file.html. The monthly GPCP data can be accessed from https://climatedataguide.ucar.edu/climate-data/gpcp-monthly-global-precipitation-climatology-project.

Acknowledgments

This work is supported by National Natural Science Foundation of China (Grant 42088101) and the Science and Technology Commission of Shanghai Municipality, China (23DZ1204703).

Conflict of interest

The authors declare that they have no known competing financial interests or personal relationships that could have appeared to influence the work reported in this paper.

Author contributions

Jiuwei Zhao 0000-0001-9146-7500
Conceptualization (equal), Data curation (lead), Formal analysis (equal), Writing – original draft (lead)

Ruifen Zhan 0000-0001-7209-0904
Conceptualization (equal), Formal analysis (equal), Funding acquisition (lead), Supervision (equal), Writing – review & editing (lead)

Yue Li 0009-0000-1553-9349
Data curation (supporting), Methodology (supporting), Visualization (equal)

Yuqing Wang 0000-0002-1691-8161
Supervision (equal), Writing – review & Editing (equal)

Weiyi Sun 0000-0001-9043-706X
Data curation (supporting), Visualization (supporting)

References

Altman J, Saurer M, Dolezal J, Maredova N, Song J-S, Ho C-H and Treydte K 2021 Large volcanic eruptions reduce landfalling tropical cyclone activity: evidence from tree rings *Sci. Total Environ.* **775** 145899

Ashok K, Guan Z and Yamagata T 2003 A look at the relationship between the ENSO and the Indian Ocean dipole *J. Meteorol. Soc. Japan II* **81** 41–56

Benton B N, Alessi M J, Herrera D A, Li X, Carrillo C M and Ault T R 2022 Minor impacts of major volcanic eruptions on hurricanes in dynamically-downscaled last millennium simulations *Clim. Dyn.* **59** 1597–615

Camargo S J, Emanuel K A and Sobel A H 2007 Use of a genesis potential index to diagnose ENSO effects on tropical cyclone genesis *J. Clim.* **20** 4819–34

Camargo S J and Polvani L M 2019 Little evidence of reduced global tropical cyclone activity following recent volcanic eruptions *npj Clim. Atmos. Sci.* **2** 14

Chai J, Liu F, Xing C, Wang B, Gao C, Liu J and Chen D 2020 A robust equatorial Pacific westerly response to tropical volcanism in multiple models *Clim. Dyn.* **55** 3413–29

Chand S S *et al* 2022 Declining tropical cyclone frequency under global warming *Nat. Clim. Change* **12** 655–61

Chen Z, Zhou T, Chen X, Zhang W, Zhang L, Wu M and Zou L 2022 Observationally constrained projection of Afro-Asian monsoon precipitation *Nat. Commun.* **13** 2552

Chiacchio M, Pausata F S R, Messori G, Hannachi A, Chin M, Önskog T, Ekman A M L and Barrie L 2017 On the links between meteorological variables, aerosols, and tropical cyclone frequency in individual ocean basins *J. Geophys. Res. Atmos.* **122** 802–22

Danabasoglu G *et al* 2020 The community earth system model version 2 (CESM2) *J. Adv. Model. Earth Syst.* **12** e2019MS001916

Delworth T L *et al* 2020 SPEAR: the next generation GFDL modeling system for seasonal to multidecadal prediction and projection *J. Adv. Model. Earth Syst.* **12** e2019MS001895

Dogar M M, Hermanson L, Scaife A A, Visioni D, Zhao M, Hoteit I, Graf H-F, Dogar M A, Almazroui M and Fujiwara M 2023 A review of El Niño Southern oscillation

linkage to strong volcanic eruptions and post-volcanic winter warming *Earth Syst. Environ.* **7** 15–42
Eddebbar Y A, Rodgers K B, Long M C, Subramanian A C, Xie S-P and Keeling R F 2019 El Niño–like physical and biogeochemical ocean response to tropical eruptions *J. Clim.* **32** 2627–49
Emanuel K 2018 100 years of progress in tropical cyclone research *Meteorol. Monogr.* **59** 15.1–15.68
Emanuel K and Nolan D S 2004 Tropical cyclone activity and the global climate system *26th Conf. Hurricanes and Tropical Meteorology* (*Miami, Florida*) (American Meteorological Society) pp 240–1
Evan A T 2012 Atlantic hurricane activity following two major volcanic eruptions *J. Geophys. Res. Atmos.* **117** 2011JD016716
Eyring V, Bony S, Meehl G A, Senior C A, Stevens B, Stouffer R J and Taylor K E 2016 Overview of the coupled model intercomparison project phase 6 (CMIP6) experimental design and organization *Geosci. Model Dev.* **9** 1937–58
Fadnavis S, Müller R, Chakraborty T, Sabin T P, Laakso A, Rap A, Griessbach S, Vernier J-P and Tilmes S 2021 The role of tropical volcanic eruptions in exacerbating Indian droughts *Sci. Rep.* **11** 2714
Gill A E 1980 Some simple solutions for heat-induced tropical circulation *Q. J. R. Meteorol. Soc.* **106** 447–62
Guevara-Murua A, Hendy E J, Rust A C and Cashman K V 2015 Consistent decrease in North Atlantic tropical cyclone frequency following major volcanic eruptions in the last three centuries *Geophys. Res. Lett.* **42** 9425–32
Haarsma R J *et al* 2016 High resolution model intercomparison project (HighResMIP v1.0) for CMIP6 *Geosci. Model Dev.* **9** 4185–208
Hersbach H *et al* 2020 The ERA5 global reanalysis *Q. J. R. Meteorol. Soc.* **146** 1999–2049
Hodges K, Cobb A and Vidale P L 2017 How well are tropical cyclones represented in reanalysis datasets? *J. Clim.* **30** 5243–64
Huang B, Thorne P W, Banzon V F, Boyer T, Chepurin G, Lawrimore J H, Menne M J, Smith T M, Vose R S and Zhang H-M 2017 Extended reconstructed sea surface temperature, version 5 (ERSSTv5): upgrades, validations, and intercomparisons *J. Clim.* **30** 8179–205
Huffman G J, Adler R F, Arkin P, Chang A, Ferraro R, Gruber A, Janowiak J, McNab A, Rudolf B and Schneider U 1997 The global precipitation climatology project (GPCP) combined precipitation dataset *Bull. Am. Meteorol. Soc.* **78** 5–20
Huffman G J, Adler R F, Behrangi A, Bolvin D T, Nelkin E J, Gu G and Ehsani M R 2023 The new version 3.2 global precipitation climatology project (GPCP) monthly and daily precipitation products *J. Clim.* **36** 7635–55
Hurrell J W, Holland M M, Gent P R, Ghan S, Kay J E and Kushner P J 2013 The community earth system model
Iles C E, Hegerl G C, Schurer A P and Zhang X 2013 The effect of volcanic eruptions on global precipitation *J. Geophys. Res. Atmos.* **118** 8770–86
Jin F-F 1997 An equatorial ocean recharge paradigm for ENSO. Part I: conceptual model *J. Atmos. Sci.* **54** 811–29
Jin F-F, Boucharel J and Lin I-I 2014 Eastern Pacific tropical cyclones intensified by El Niño delivery of subsurface ocean heat *Nature* **516** 82–85
Khodri M *et al* 2017 Tropical explosive volcanic eruptions can trigger El Niño by cooling tropical Africa *Nat. Commun.* **8** 778
Knapp K R, Kruk M C, Levinson D H, Diamond H J and Neumann C J 2010 The International Best Track Archive for Climate Stewardship (IBTrACS): unifying tropical cyclone data *Bull. Am. Meteorol. Soc.* **91** 363–76
Knutson T *et al* 2019 Tropical cyclones and climate change assessment: part i: detection and attribution *Bull. Am. Meteorol. Soc.* **100** 1987–2007
Li M, Gao F, Nie Z, Sun B, Liu Y and Gong X 2024 Investigation into the methodology and implementation of life cycle engineering under China's carbon reduction target in the process industry *Engineering* **40** 87–99
Li W, Li L and Deng Y 2015 Impact of the Interdecadal Pacific Oscillation on tropical cyclone activity in the North Atlantic and eastern North Pacific *Sci. Rep.* **5** 12358
Liu F, Chai J, Wang B, Liu J, Zhang X and Wang Z 2016 Global monsoon precipitation responses to large volcanic eruptions *Sci. Rep.* **6** 24331
Liu F, Gao C, Chai J, Robock A, Wang B, Li J, Zhang X, Huang G and Dong W 2022 Tropical volcanism enhanced the East Asian summer monsoon during the last millennium *Nat. Commun.* **13** 3429
Liu F, Xing C, Sun L, Wang B, Chen D and Liu J 2018 How do tropical, Northern Hemispheric, and Southern Hemispheric volcanic eruptions affect ENSO under different initial ocean conditions? *Geophys. Res. Lett.* **45** 13,041–9
Lu F *et al* 2020 GFDL's SPEAR seasonal prediction system: initialization and ocean tendency adjustment (OTA) for coupled model predictions *J. Adv. Model. Earth Syst.* **12** e2020MS002149
Matsuno T 1966 Quasi-geostrophic motions in the equatorial area *J. Meteorol. Soc. Japan II* **44** 25–43
Murakami H, Delworth T L, Cooke W F, Zhao M, Xiang B and Hsu P-C 2020 Detected climatic change in global distribution of tropical cyclones *Proc. Natl Acad. Sci.* **117** 10706–14
Murakami H, Levin E, Delworth T L, Gudgel R and Hsu P-C 2018 Dominant effect of relative tropical Atlantic warming on major hurricane occurrence *Science* **362** 794–9
Murakami H, Mizuta R and Shindo E 2012 Future changes in tropical cyclone activity projected by multi-physics and multi-SST ensemble experiments using the 60 km-mesh MRI-AGCM *Clim. Dyn.* **39** 2569–84
Murakami H and Wang B 2010 Future change of North Atlantic tropical cyclone tracks: projection by a 20 km-mesh global atmospheric model *J. Clim.* **23** 2699–721
Murakami H, Wang B, Li T and Kitoh A 2013 Projected increase in tropical cyclones near Hawaii *Nat. Clim. Change* **3** 749–54
Nicholls N 1988 Low latitude volcanic eruptions and the El Niño-Southern Oscillation *J. Climatol.* **8** 91–95
Paik S, Min S-K, Iles C E, Fischer E M and Schurer A P 2020 Volcanic-induced global monsoon drying modulated by diverse El Niño responses *Sci. Adv.* **6** eaba1212
Patricola C M, Chang P and Saravanan R 2016 Degree of simulated suppression of Atlantic tropical cyclones modulated by flavour of El Niño *Nat. Geosci.* **9** 155–60
Pausata F S R and Camargo S J 2019 Tropical cyclone activity affected by volcanically induced ITCZ shifts *Proc. Natl Acad. Sci.* **116** 7732–7
Predybaylo E, Stenchikov G, Wittenberg A T and Osipov S 2020 El Niño/Southern oscillation response to low-latitude volcanic eruptions depends on ocean pre-conditions and eruption timing *Commun. Earth Environ.* **1** 12
Rayner N A, Parker D E, Horton E B, Folland C K, Alexander L V, Rowell D P, Kent E C and Kaplan A 2003 Global analyses of sea surface temperature, sea ice, and night marine air temperature since the late nineteenth century *J. Geophys. Res. Atmos.* **108** 2002JD002670
Robock A 2000 Volcanic eruptions and climate *Rev. Geophys.* **38** 191–219
Sato M, Hansen J E, McCormick M P and Pollack J B 1993 Stratospheric aerosol optical depths, 1850–1990 J *Geophys. Res. Atmos.* **98** 22987–94
Showman A P and Polvani L M 2010 The Matsuno-Gill model and equatorial superrotation *Geophys. Res. Lett.* **37** 2010GL044343
Slivinski L C *et al* 2019 Towards a more reliable historical reanalysis: improvements for version 3 of the twentieth

century reanalysis system *Q. J. R. Meteorol. Soc.* **145** 2876–908

Sobel A H, Wing A A, Camargo S J, Patricola C M, Vecchi G A, Lee C-Y and Tippett M K 2021 Tropical cyclone frequency *Earth's Future* **9** e2021EF002275

Song K, Zhao J, Zhan R, Tao L and Chen L 2022 Confidence and uncertainty in simulating tropical cyclone long-term variability using the CMIP6-HighResMIP *J. Clim.* **35** 6431–51

Vimont D J and Kossin J P 2007 The Atlantic meridional mode and hurricane activity *Geophys. Res. Lett.* **34** 2007GL029683

Walsh K J E *et al* 2015 Hurricanes and climate: the U.S. CLIVAR working group on hurricanes *Bull. Am. Meteorol. Soc.* **96** 997–1017

Wang B and Chan J C L 2002 How strong ENSO events affect tropical storm activity over the western North Pacific *J. Clim.* **15** 1643–58

Xiang B *et al* 2022 S2S prediction in GFDL SPEAR: MJO diversity and teleconnections *Bull. Am. Meteorol. Soc.* **103** E463–84

Yan Q, Korty R, Zhang Z and Wang H 2019 Evolution of tropical cyclone genesis regions during the Cenozoic era *Nat. Commun.* **10** 3076

Yan Q, Zhang Z and Wang H 2017 Divergent responses of tropical cyclone genesis factors to strong volcanic eruptions at different latitudes *Clim. Dyn.* **50** 2121–36

Zanchettin D *et al* 2016 The model intercomparison project on the climatic response to volcanic forcing (VolMIP): experimental design and forcing input data for CMIP6 *Geosci. Model Dev.* **9** 2701–19

Zhang W, Vecchi G A, Murakami H, Villarini G, Delworth T L, Yang X and Jia L 2018 Dominant role of Atlantic multidecadal oscillation in the recent decadal changes in western North Pacific tropical cyclone activity *Geophys. Res. Lett.* **45** 354–62

Zhang W, Vecchi G A, Villarini G, Murakami H, Rosati A, Yang X, Jia L and Zeng F 2017 Modulation of western North Pacific tropical cyclone activity by the Atlantic meridional mode *Clim. Dyn.* **48** 631–47

Zhao J, Wang F, Zhan R, Guo Y, Huang X and Liu C 2023 How does tropical cyclone genesis frequency respond to a changing climate? *Geophys. Res. Lett.* **50** e2023GL102879

Zhao J, Zhan R and Wang Y 2020a Different responses of tropical cyclone tracks over the western North Pacific and North Atlantic to two distinct sea surface temperature warming patterns *Geophys. Res. Lett.* **47** e2019GL086923

Zhao J, Zhan R, Wang Y, Jiang L and Huang X 2022 A multiscale-model-based near-term prediction of tropical cyclone genesis frequency in the Northern Hemisphere *J. Geophys. Res. Atmos.* **127** e2022JD037267

Zhao J, Zhan R, Wang Y and Tao L 2016 Intensified interannual relationship between tropical cyclone genesis frequency over the Northwest Pacific and the SST gradient between the Southwest Pacific and the western Pacific warm pool since the Mid-1970s *J. Clim.* **29** 3811–30

Zhao J, Zhan R, Wang Y, Xie S-P and Wu Q 2020b Untangling impacts of global warming and Interdecadal Pacific Oscillation on long-term variability of North Pacific tropical cyclone track density *Sci. Adv.* **6** eaba6813

Zhao J, Zhan R, Wang Y and Xu H 2018 Contribution of the Interdecadal Pacific Oscillation to the recent abrupt decrease in tropical cyclone genesis frequency over the western North Pacific since 1998 *J. Clim.* **31** 8211–24

Zhao M, Held I M, Lin S-J and Vecchi G A 2009 Simulations of global hurricane climatology, interannual variability, and response to global warming using a 50 km resolution GCM *J. Clim.* **22** 6653–78

Zhou T, Zuo M and Man W 2023 Recent advances and future avenues in examining the impacts of volcanic aerosols on climate *Chin. Sci. Bull.* **69** 230–52

Zhou Y, Zhao J, Zhan R, Chen P, Wu Z and Wang L 2021 A logistic-growth-equation-based intensity prediction scheme for western North Pacific tropical cyclones *Adv. Atmos. Sci.* **38** 1750–62

Zhu F, Emile-Geay J, Anchukaitis K J, Hakim G J, Wittenberg A T, Morales M S, Toohey M and King J 2022 A re-appraisal of the ENSO response to volcanism with paleoclimate data assimilation *Nat. Commun.* **13** 747